Supporting Information

to

Polymer Brush-Grafted Cellulose Nanocrystals for the Synthesis of Porous Carbon-Coated Titania Nanocomposites

Yen Theng Cheng,[1,3] *Qingbo Xia,*[2,3] *Hongwei Liu,*[4] *Marcello B. Solomon,*[2] *Chris D. Ling,*[2,3] *Markus Müllner*[1,3,*]

[1]Key Centre for Polymers and Colloids, School of Chemistry, The University of Sydney, Sydney, NSW 2006, Australia; [2]School of Chemistry, The University of Sydney, Sydney, NSW 2006, Australia; [3]The University of Sydney Nano Institute (Sydney Nano), Sydney, NSW 2006, Australia; [4]Sydney Microscopy & Microanalysis, the University of Sydney node of Microscopy Australia, Sydney, NSW 2006, Australia.

Email correspondence to markus.muellner@sydney.edu.au

Table of Contents

Materials

Pristine cellulose nanocrystals (CNCs) were extracted from Whatman No.1 filter papers according to published procedure.[1] 2-(Dimethylamino)ethyl methacrylate (DMAEMA, 98%), 1,1,4,7,10,10-hexamethyltriethylenetetramine (HMTETA, 97%), ethyl *α*-bromoisobutyrate (EBiB, 98%), *α*-bromoisobutyryl bromide (α-BiBB, 98%), titanium(IV) *bis*(ammonium lactato)dihydroxide (TALH) solution (50 wt% in H_2O), nanosized anatase particles (P25, 99.7%), poly(vinylidene fluoride) (PVDF, >99%), battery grade lithium hexafluorophosphate ($LiPF_6$) electrolyte solution (1.0 M) in ethylene carbonate/diethyl carbonate (1:1) were purchased from Sigma Aldrich. 1-Methyl 2-pyrrolidinone (NMP, > 99%) and carbon black (Super P® Conductive, 99+%, metals basis) were purchased from Alfa Aesar. Copper(I) chloride, triethylamine and 4-dimethylaminopyridine were purchased from Merck. DMAEMA were purified by passing through a column of neutral aluminium oxide for inhibitor removal. All remaining chemicals were used as received. Deuterated chloroform ($CDCl_3$, 99%) was purchased from Cambridge Isotopes Laboratories. Coin cell sets, including stainless steel CR2032 top and bottom caps, wave springs, spacers and 19 mm Celgard polypropylene films (separators) were purchased from MTI.

Methods

Proton nuclear magnetic resonance (^{1}H NMR) spectra were recorded in $CDCl_3$ using a 300 MHz Bruker Avance system at 300 K.

Elemental analysis of the Br content by mass in CNC-Br polyinitiator sample was performed by the Pascher Microanalytical Lab in Germany.

Fourier-transform infrared spectroscopy (FTIR) measurements. All CNC and surface-modified CNCs were analysed using a PerkinElmer Spectrum Two FTIR spectrometer. All spectra were recorded from 4000 to 400 cm^{-1} with a spectral resolution of 1 cm^{-1} and 16 scans.

Size exclusion chromatography (SEC) was performed on an UFLC Shimadzu Prominence SEC system with a pair of PhenogelTM columns (5 mm, 104, and 105Å) calibrated with PMMA standards and running at a flow rate of 1 mL min^{-1} at 50 ºC. Dimethylacetamide (DMAc) and BHT/LiBr at 0.05 wt%. GPC sample containing CNC-*g*-PDMAEMA and sacrificial PDMAEMA were dispersed in DMAc and passed through a 220 nm nylon filter several times prior to injection.

Thermogravimetric analysis (TGA) was performed on a TA Instruments Discovery thermogravimetric analyser. Solid samples were heated under a flow of air or argon from room

temperature to 600 ºC at a ramp rate of 5 ºC min^{-1}. The samples were held at 100 ºC for 10 min to remove residual solvent.

Scanning electron microscopy (SEM) was performed on a Zeiss Sigma HD FEG SEM. Images were collected at a working distance of 3.5–5.0 mm at an accelerating voltage of 3 kV. All studied materials were sputtered with gold (5 nm) prior to SEM imaging.

Transmission electron microscopy (TEM) was performed on a JEM-2100CR instrument equipped with a 5k × 4k CMOS camera (EMSIS). Images were collected in bright-field mode with a spot size of 3 with diffraction contrast enhanced by using an objective lens aperture with a size of 20 μm, at an accelerating voltage of 200 kV. Each sample was well-dispersed in water (10 mg mL^{-1}) and drop-casted onto an ultrathin continuing carbon film that was supported by a copper grid. Pristine CNC was negatively stained with uranyl acetate solution (2%) for 2 min prior to imaging. The remaining samples were imaged without any staining.

Powder X-ray diffraction (PXRD) data were collected on a PANalaytical X-pert Pro powder diffractometer, with non-monochromated Cu K_α X-ray radiation (λ = 1.5406 Å) and a PIXcel1D detector in continuous scanning mode at a speed of 1.26º min^{-1} and a step size of 0.001º over the 2θ angle range 5–80º. Average crystallite sizes of TiO_2/C nanotubes and TiO_2 nanorods were estimated using Debye-Scherrer equation by selecting the diffraction peaks at 2θ = 25.5º, 38.4º and 48.2º.

Raman spectroscopy was performed using a Renishaw InVia Qontor confocal Raman Microscope (Renishaw plc., Wotton-under-Edge, UK), equipped with a continuous wave, diode-pumped solid-state laser (Renishaw plc., Wotton-under-Edge, UK) emitting at 532 nm. Spectra were recorded using the × 50/0.75 NA over the spectral range of 100–3200 cm^{-1} with the accumulation of one to five scans, 10 s exposure and a laser power of ~0.15 mW. Where necessary, spectra were processed using Renishaw WiRE^{TM} (Version 5.4) to remove cosmic rays.

N_2 physisorption isotherms were measured using a 3-Flex supplied by Micromeritics Instruments Inc. The sample (~50–100 mg) was loaded into a glass analysis tube and outgassed for 36 h under vacuum at 100 ºC, prior to analysis. The adsorption and desorption isotherms were measured at 77 K, and the data were analysed using the Brunauer-Emmett-Teller (BET) models to determine the surface area. Pore size distributions were calculated using Density Functional Theory (DFT) cylindrical pore model for oxide surfaces in the Micromeritics MicroActive Software Package Version 4.01.

Coin cell fabrication and testing. A homogenous electrode slurry was prepared by mixing the nanostructured TiO_2/C or TiO_2 (70 mg, the active material), carbon black (15 mg, the electron-conducting additive), polyvinylidene fluoride (PVDF, 15 mg, the binder) and *N*-methyl-2-pyrrolidone (NMP, 2 mL, the solvent) overnight. The slurry was then tape-casted onto a copper foil (the current collector) to form an electrode film. After being dried overnight at 80 ºC, the film was cut into the electrode disks with a diameter of 16 mm. The disks were then completely dried under vacuum at 120 ºC for 5 h before being transferred into an argon-filled glovebox for assembling coin cells. The loading density of the active material on each disk is ~1.60 mg cm^{-2}, and the thickness of its film is 20 μm. CR2032 coin cells were then assembled inside the glovebox using lithium metal chips (diameter: 16mm) as the counter electrodes, three-layer polypropylene/polyethylene/polypropylene (PP/PE/PP) composite films (diameter: 19 mm) as the separators, and $LiPF_6$ (1 M) in ethyl carbonate and diethyl carbonate (50/50; v/v) as the electrolyte. Finally, galvanostatic charge-discharge measurements (0.1–5 C, 1C = 335 mAh g^{-1}) were performed on the coin cells on a Neware battery testing system in a voltage window of 0.01–2.5 V at room temperature.

Supporting Results and Discussion

S1. TEM of pristine CNC

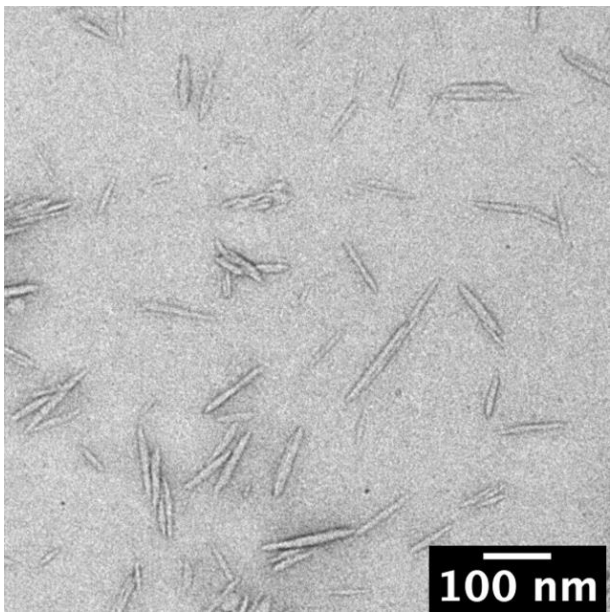

Figure S1. TEM image of the pristine CNCs isolated from Whatman No.1 filter paper treated by sulfuric acid hydrolysis.

S2. XRD of pristine CNC and CNC-Br

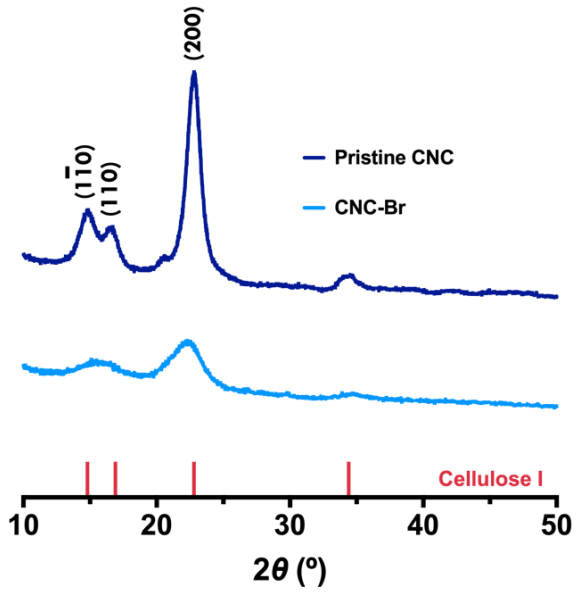

Figure S2. PXRD data for pristine CNC and CNC-Br. The pink vertical ticks designate the characteristic Bragg diffraction peaks of cellulose I.

S3. Degree of substitution of ATRP initiator on CNC surface

Please refer to the following calculation for the degree of substitution (DS) calculation.

According to Malho *et al.*,[2] the DS of ATRP initiator on CNC surface can be calculated by following the equation below:

$$\mathrm{DS} = \frac{\text{No. of cellulose unit } (\mathrm{N_{all}})}{\text{No. of surface cellulose units } (\mathrm{N_{surf}})} \times \frac{\text{No. of initiator, n(Ini)}}{\text{No. anhydroglucose units, n(AnGlu)}}$$

Using elemental analysis, CNC-Br sample was determined to have a bromine content, f(Br), of 6.66 wt%. The molar concentration of bromine correlates with the molar concentration of initiators, n(Ini), given:

$$\mathrm{n(Ini)} = \frac{\mathrm{f(Br)}}{\text{atomic mass(Br)}} = \frac{0.066}{79.9\ \mathrm{g/mol}} = 8.3 \times 10^{-2}\ \mathrm{mol/g}$$

Since the molecular weight per initiator, M(Ini), is 166 g/mol, the initiator weight fraction, f(Ini) is therefore:

$$\mathrm{f(Ini)} = \mathrm{f(Ini)} \times \mathrm{M(Ini)} = 8.3 \times 10^{-2}\ \mathrm{mol/g} \times 166\ \mathrm{g/mol} = 0.137$$

Given that the molar amount of anhydroglucose units per gram, n(AnGlu), can be defined by:

$$\mathrm{n(AnGlu)} = \frac{1 - \mathrm{f(Ini)}}{\text{molecular weight of AnGlu}} = \frac{1 - 0.14}{162\ \mathrm{g/mol}} = 5.3 \times 10^{-3}\ \mathrm{mol/g}$$

The molar ratio of initiator to anhydroglucose units in CNC-Br is then calculated to be:

$$\frac{\mathrm{n(Ini)}}{\mathrm{n(AnGlu)}} = \frac{8.3 \times 10^{-2}\ \mathrm{mol/g}}{5.3 \times 10^{-3}\ \mathrm{mol/g}} = 0.15$$

Since the ratio of surface cellulose chains to all chains is approximated to be 0.39,[3] the DS of ATRP initiator on CNC surface is therefore:

$$\mathrm{DS} = \frac{1}{0.39} \times 0.15 = 0.39$$

S4. Polymerisation kinetics of SI-ATRP of DMAEMA from CNC-Br

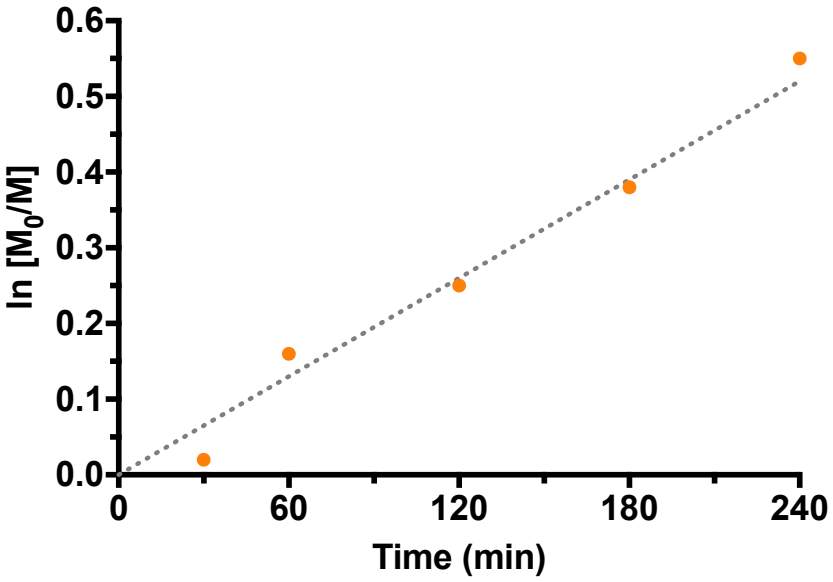

Figure S3. First-order kinetic plot for the SI-ATRP of DMAEMA from CNC-Br polyinitiator monitored by ^{1}H NMR spectroscopy.

S5. SEC of sacrificial PDMAEMA

PDMAEMA was polymerised from CNC-Br in the presence of a sacrificial initiator (EBiB). The resultant sacrificial PDMAEMA was analysed using SEC.

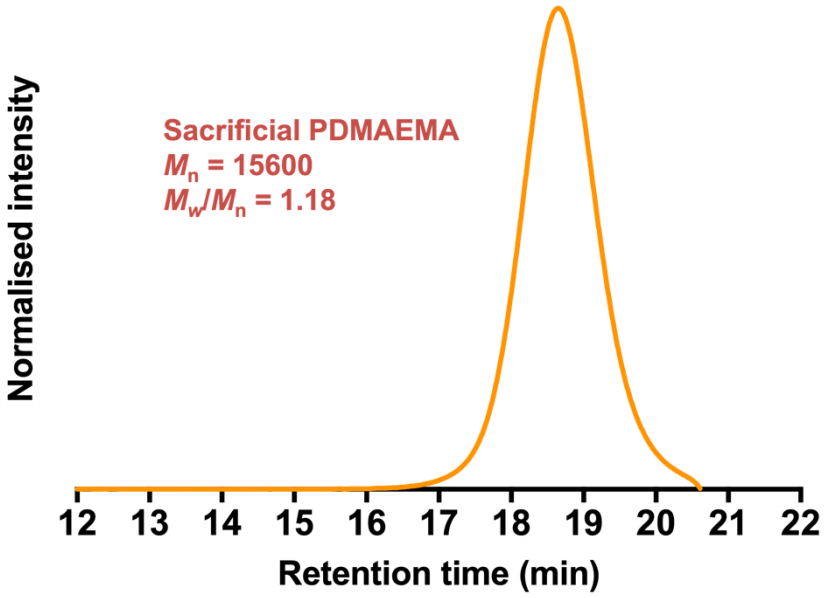

Figure S4. Size exclusion chromatograms of sacrificial PDMAEMA measured using dimethylacetamide (DMAc) as the eluent.

S6. HR-TEM of TiO_2/C and TiO_2 nanomaterials

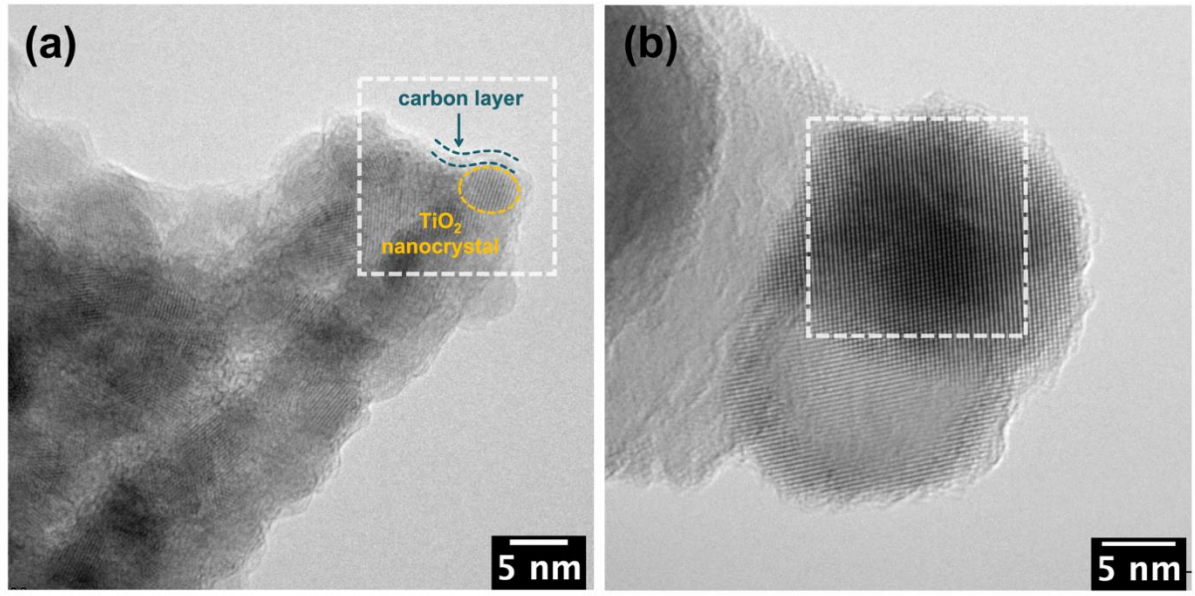

Figure S5. HR-TEM image of (a) TiO_2/C and (b) TiO_2 nanomaterials, showing the carbon layer atop the TiO_2/C nanotubes and the lattice fringe of pure TiO_2 nanorods, respectively.

S7. N_2-physisorption analysis

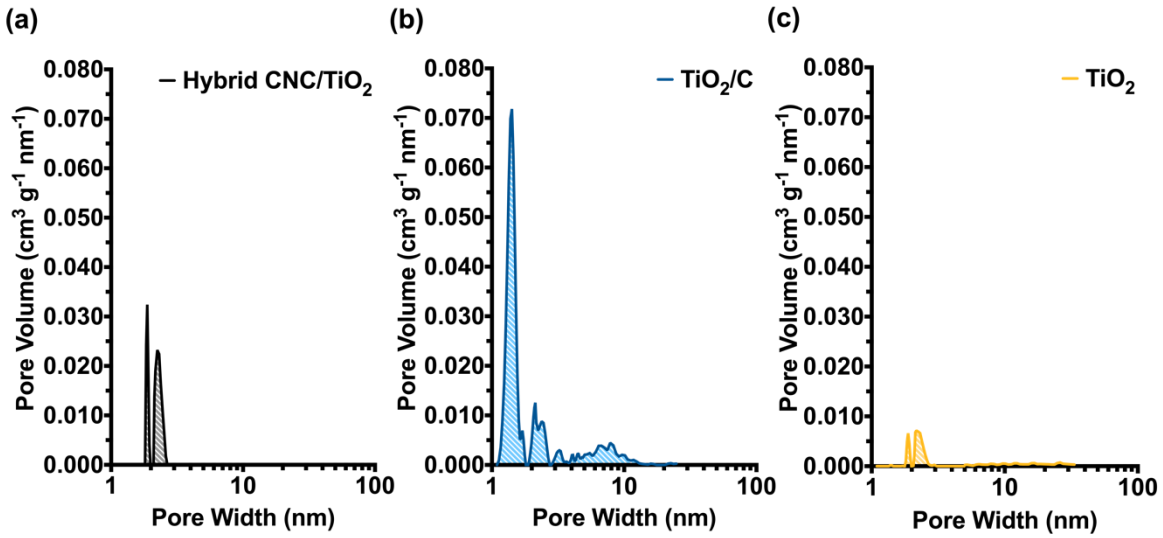

Figure S6. Pore size distributions of the (a) hybrid CNC/TiO_2, (b) TiO_2/C nanotubes and (c) TiO_2 nanorods, as determined by applying the DFT method.

The N_2 physisorption isotherm of TiO_2/C nanorods exhibited a Type II isotherm behavior with an H4 hysteresis loop, indicative of mesoporous and macroporous that formed during the carbonisation process. Contrary to that, the hybrid CNC/TiO_2 and TiO_2 nanorods displayed Type II isotherm behaviours with an H3 hysteresis loop, which are indicative of nonporous or macroporous materials. The improved porosity of the carbon-coated material was also reflected by the sorption of N_2 at lower relative pressures from 0.1 to 1.0 mmol g^{-1}. This is also in harmony with the pore size distribution of the material that showed a large volume of mesopores that ranged from 2–30 nm.

S8. Raman spectroscopy

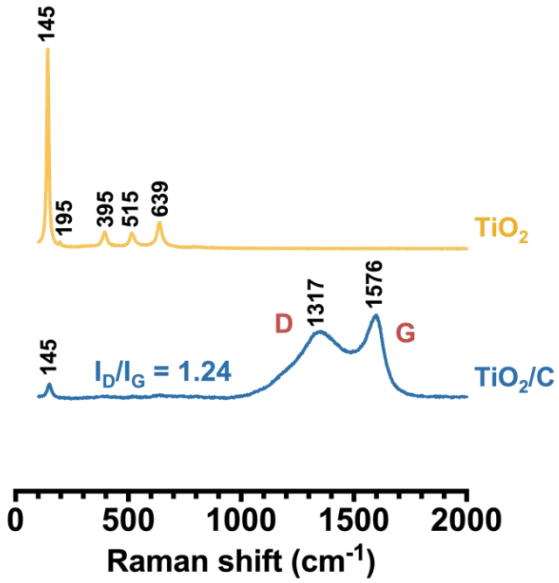

Figure S7. Raman spectra of TiO_2/C nanotubes (blue) and TiO_2 nanorods (yellow).

S9. Additional electrochemical performance data and discussion

The discharge and charge voltage profiles of TiO_2/C nanotubes are characterised by steep sloping curves, which indicate their lithiation-delithiation mechanisms that exhibit capacitance behaviour (Figure 4a). Such behaviour typically becomes more dominant for electrode materials with larger surface areas as the crystallite size decreases.[4] The initial short, steep slope in each discharge voltage profile corresponds to the insertion of Li^+ ions into the anatase material, forming the Li-poor tetragonal Li_xTiO_2 ($x << 0.5$). The steep slope was immediately followed by a voltage plateau at ~1.8 V *vs* Li/Li^+, corresponding to the transition from the tetragonal Li_xTiO_2 ($x << 0.5$) phase to the orthorhombic $Li_{0.5}TiO_2$ (i.e., the first two-phase transition of the anatase). Between 1.8–0.01 V *vs* Li/Li^+, the long descending slope is attributed to (i) the transition of the orthorhombic $Li_{0.5}TiO_2$ phase to the tetragonal Li-rich Li_xTiO_2 ($0.5 < x \leq 1$) phase (i.e., the second two-phase transition of the anatase), and (ii) the lithiation of the amorphous carbon within the TiO_2/C nanotubes. The phase transitions occurred in reverse order during the charging process with small over-potentials e.g., the reversed first two-phase transition from the orthorhombic $Li_{0.5}TiO_2$ phase to the tetragonal Li_xTiO_2 ($x << 0.5$) phase accompanied by a voltage plateau, which appeared at an increased voltage to ~2.0 V *vs* Li/Li^+., For our TiO_2 nanomaterials without carbon, their voltage plateaus were observed to be reducing in length over cycling (Figure S8-1a) which is attributed to their dramatically lower

electrochemical activities than the as-synthesised TiO_2/C nanotubes. The crystallite size of the TiO_2 nanomaterials without carbon (~36.4 nm) is significantly larger than that of the as-synthesised TiO_2/C (~4.6 nm), while the former also has a much smaller surface area (16 vs. 111 m^2 g^{-1}). These two factors lead to extreme difficulties for Li^+ ions and electrons diffusing across the anatase bulk and sluggish lithiation-delithiation kinetics.

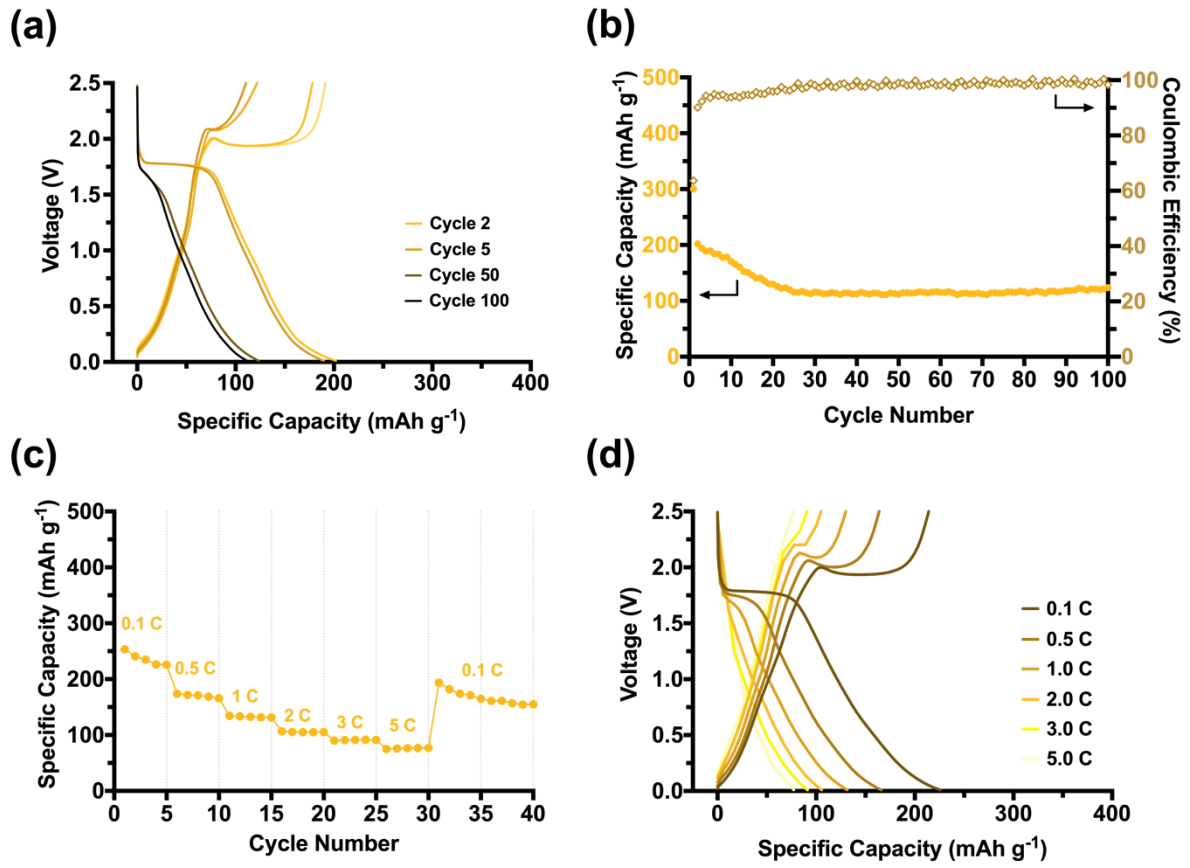

Figure S8-1. The electrochemical performance of bare TiO_2 nanorods as LIB anodes: (a) Galvanostatic charge/discharge voltage profiles in cycles 2, 5, 50 and 100 at 0.1C, (b) cycling performance over 100 cycles at 0.1C (the plot fluctuation observed in the specific capacity in (b) is caused by the changes in room temperature during battery cycling). (c) Rate performance and (d) galvanostatic charge/discharge curves of TiO_2 nanorods at various C-rates.

As shown in Figure S8-1a, bare TiO_2 nanorods delivered a capacity of 202 mAh g^{-1} in the second cycle. Even though the capacity loss between the 2nd and 5th cycles was only 13 mAh g^{-1}, the capacity decreased substantially from the 5th cycle (189 mAh g^{-1}) to 25th cycle (115 mAh g^{-1}) with a capacity loss rate of 39.2%. Figure S8-1c shows the rate capability of bare TiO_2 nanorods. Their capacities were significantly lower than those of TiO_2/C nanotubes when subjected to the same current density. Additionally, when the current density was switched back

from 5.0C to 0.1C, the capacity did not recover to the same high levels as before the rate capability test. The commercial nano-sized anatase (P25) delivered a capacity (~320 mAh g^{-1}; Figure S8-2a) in the second cycle, which was higher than our calcined TiO_2 nanorods (~200 mAh g^{-1}; Figure S8-1a) but lower than our TiO_2/C nanotubes (~390 mAh g^{-1}; Figure 5a). However, the commercial anatase (compared to TiO_2/C) showed an extremely poor cycling stability due to its larger particle size (~25 nm) and its non-templated morphology.

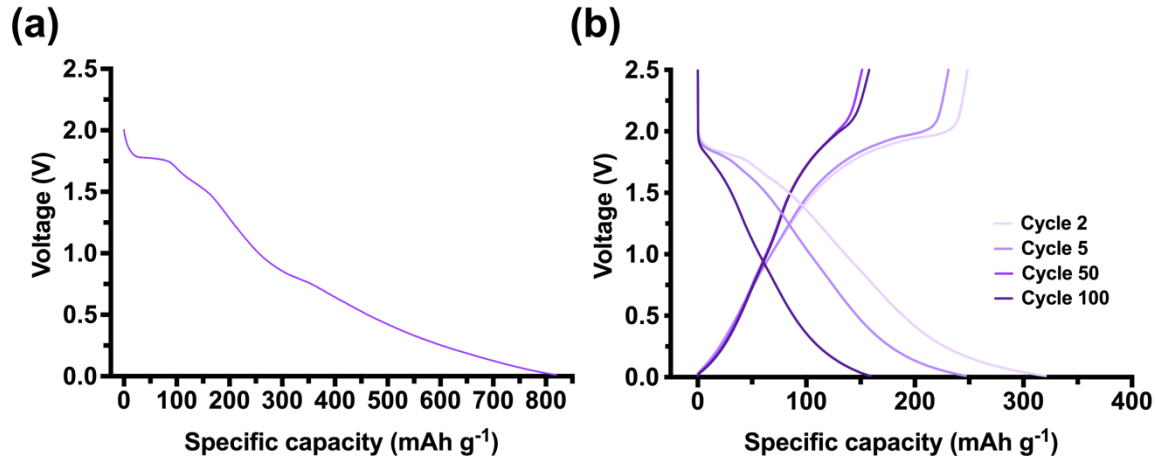

Figure S8-2. (a) Initial discharge and (b) charge-discharge voltage profiles of the battery prepared using commercial P25 anatase nanoparticles (particle size: 25 nm). Note that cycles 50 and 100 show two overlapping discharge voltage curves.

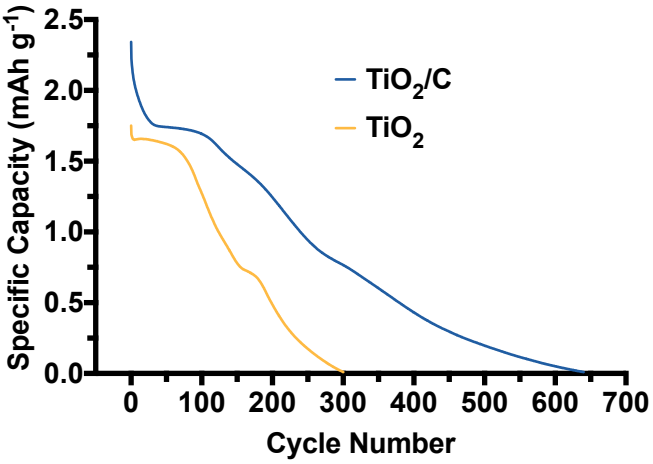

Figure S8-3. Initial voltage discharge profiles of TiO_2/C nanotubes (red) and TiO_2 nanorods (yellow).

References

1 C. D. Edgar and D. G. Gray, *Cellulose*, 2003, **10**, 299–306.

2 J.-M. Malho, M. Morits, T. I. Löbling, Nonappa, J. Majoinen, F. H. Schacher, O. Ikkala and A. H. Gröschel, *ACS Macro Lett.*, 2016, **5**, 1185–1190.

3 J. Majoinen, A. Walther, J. R. McKee, E. Kontturi, V. Aseyev, J. M. Malho, J. Ruokolainen and O. Ikkala, *Biomacromolecules*, 2011, **12**, 2997–3006.

4 C. Liu, Z. G. Neale and G. Cao, *Mater. Today*, 2016, 19, 109–123.